LETTER

doi:10.1038/nature17418

Northern Hemisphere hydroclimate variability over the past twelve centuries

Fredrik Charpentier Ljungqvist[1,2,3], Paul J. Krusic[4,5], Hanna S. Sundqvist[3,5], Eduardo Zorita[6], Gudrun Brattström[3,7] & David Frank[8]

Accurate modelling and prediction of the local to continental-scale hydroclimate response to global warming is essential given the strong impact of hydroclimate on ecosystem functioning, crop yields, water resources, and economic security[1–4]. However, uncertainty in hydroclimate projections remains large[5–7], in part due to the short length of instrumental measurements available with which to assess climate models. Here we present a spatial reconstruction of hydroclimate variability over the past twelve centuries across the Northern Hemisphere derived from a network of 196 at least millennium-long proxy records. We use this reconstruction to place recent hydrological changes[8,9] and future precipitation scenarios[7,10,11] in a long-term context of spatially resolved and temporally persistent hydroclimate patterns. We find a larger percentage of land area with relatively wetter conditions in the ninth to eleventh and the twentieth centuries, whereas drier conditions are more widespread between the twelfth and nineteenth centuries. Our reconstruction reveals that prominent seesaw patterns of alternating moisture regimes observed in instrumental data[12–14] across the Mediterranean, western USA, and China have operated consistently over the past twelve centuries. Using an updated compilation of 128 temperature proxy records[15], we assess the relationship between the reconstructed centennial-scale Northern Hemisphere hydroclimate and temperature variability. Even though dry and wet conditions occurred over extensive areas under both warm and cold climate regimes, a statistically significant co-variability of hydroclimate and temperature is evident for particular regions. We compare the reconstructed hydroclimate anomalies with coupled atmosphere–ocean general circulation model simulations and find reasonable agreement during pre-industrial times. However, the intensification of the twentieth-century-mean hydroclimate anomalies in the simulations, as compared to previous centuries, is not supported by our new multi-proxy reconstruction. This finding suggests that much work remains before we can model hydroclimate variability accurately, and highlights the importance of using palaeoclimate data to place recent and predicted hydroclimate changes in a millennium-long context[16,17].

Global warming is expected to strongly influence the hydrological cycle[2–4,18,19]. Model simulations and theory suggest an intensification of the wet–dry contrast at lower latitudes[5] and a widespread expansion of dry areas over land[3]. These projections have yet to be robustly detected in recent instrumental observations[8,9]. Furthermore, regional changes in precipitation patterns and drought intensity, in response to global warming, are challenging to predict owing to the chaotic nature of hydroclimate variability, the low spatial coherence of precipitation, and fine-scale processes related to cloud formation and precipitation, resulting in the large spread among model simulations[6,7]. From proxy evidence, we know that hydroclimate anomalies of larger amplitude and longer duration than found in modern instrumental observations have occurred in the past millennium: for example, the medieval 'megadroughts' in the western USA[20], and the monsoon failures in east Asia[21] in the fifteenth–nineteenth centuries. This strongly suggests that the instrumental period is too short to capture the full range of natural hydroclimate variability. In this light, a comprehensive aggregation and assessment of millennium-long moisture-sensitive palaeoclimate proxy data are needed to improve our knowledge of past hydroclimate variability, provide a test bed for model simulations, and facilitate the detection of anthropogenic impacts on the hydrological cycle[16].

Here, we analyse the spatio-temporal patterns of hydrological anomalies in an unprecedentedly large network of 196 hydroclimate proxy records from Northern Hemisphere land areas over the past twelve centuries. All are previously published as indicators of precipitation, drought, moisture balance, stream flow, lake level change, bog surface wetness or similar hydrological information derived from archives such as ice cores, marine sediments, lake sediments, speleothems, tree rings, and historical documentary data (Fig. 1a; Supplementary Table 1). All records span at least the past millennium, have at least two observations per century, and passed a screening procedure for geochronological dating control (Methods). Using the same selection and screening criteria, we updated and improved the temperature proxy network from ref. 15 (now 128 records), to investigate the co-variability between hydroclimate and temperature (Fig. 1b; Supplementary Table 2).

To develop a spatial reconstruction we standardized each proxy record from its original units (for example, $\delta^{18}O$, ring width, millimetres of precipitation) to an index, ranging from -2 to $+2$ standard deviations, of centennial variation (Methods). Anomalies exceeding -2 or $+2$ are considered outliers and truncated in order to minimize the influence of a few 'extreme' values. This index is interpreted as a measure of relative water availability, analogous to the Palmer Drought Severity Index (PDSI)[20,21], which permits comparisons of relative variations in moisture conditions between arid and moist regions.

This standardization is of particular importance given the different and potentially biased high- to low-frequency signal ratio in the various proxies. It essentially transforms the centennial-scale information in each proxy record to the same amplitude regardless of possible spectral biases (Methods). To extract a common spatial signal from the heterogeneous proxy data, the indices are spatially averaged over an estimated correlation decay length (latitudinally dependent) of centennial-scale hydroclimate and temperature variability, respectively, derived from model simulations and instrumental data (Methods; Extended Data Fig. 1). Unlike field reconstruction methods that rely upon teleconnections found in the instrumental period[22], our technique yields a grid of hydrological anomalies that is independent of any spatial co-variability found in gridded instrumental observations[15].

Our results reveal a general tendency towards a larger percentage of land area with relatively wetter conditions during the ninth–eleventh and twentieth centuries, whereas the twelfth–nineteenth centuries show larger areas with relatively drier conditions (Fig. 2). Centennial periods of reconstructed widespread dry conditions occurred under

[1]Department of History, Stockholm University, SE-10691 Stockholm, Sweden. [2]Centre for Medieval Studies, Stockholm University, SE-10691 Stockholm, Sweden. [3]Bolin Centre for Climate Research, Stockholm University, SE-10691 Stockholm, Sweden. [4]Navarino Environmental Observatory, GR-24001 Messinia, Greece. [5]Department of Physical Geography, Stockholm University, SE-10691 Stockholm, Sweden. [6]Helmholtz-Zentrum Geesthacht, Institute for Coastal Research, DE-21502 Geesthacht, Germany. [7]Department of Mathematics, Stockholm University, SE-10691 Stockholm, Sweden. [8]Swiss Federal Research Institute WSL, CH-8903 Birmensdorf, Switzerland.

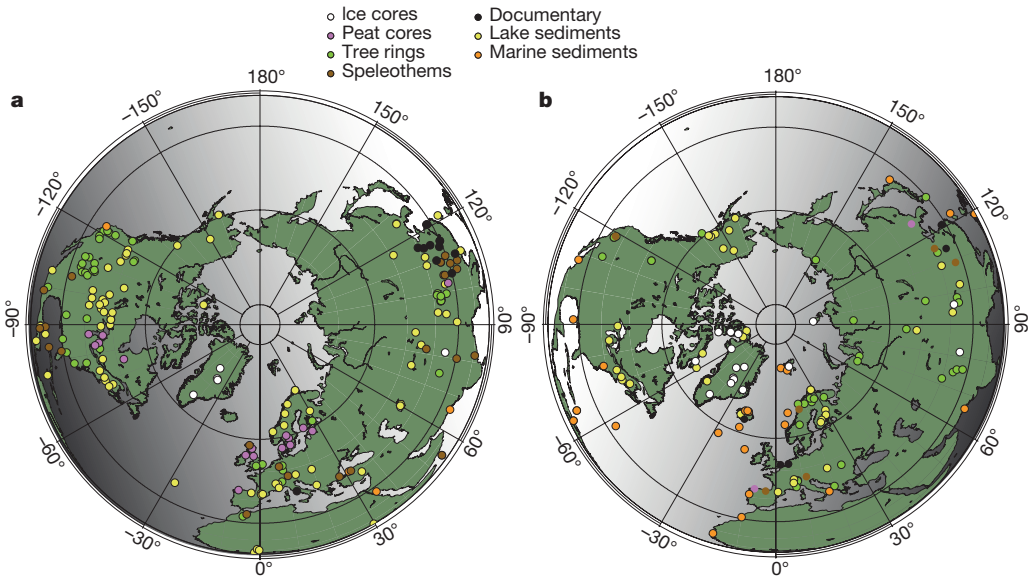

Figure 1 | Location map of the proxy records used in this study sorted by archive. a, Locations of the 196 hydrological proxy records for the past twelve centuries. **b**, Locations of the 128 temperature proxy records for the past twelve centuries. All the records cover at least the period 1000–1899. We note that some proxies share the same geographical position but are based on different types of archives.

both warm and cold climate states (Fig. 3). Notably, the dry twelfth century (with 27% reconstructed hydroclimate anomalies <-0.5) is associated with positive forcing anomalies from high solar activity and moderate volcanic activity, whereas the equally dry fifteenth century (also with 27% reconstructed hydroclimate anomalies <-0.5) coincides with negative forcing anomalies from low solar forcing and several large volcanic eruptions[23]. We identify inverse hydroclimate conditions (that is, hydroclimate dipoles) over geographically adjacent regions that persist on centennial timescales. This phenomenon has been reported in studies of instrumental data and some proxy time series for the same regions: the eastern and western Mediterranean[12]; the southwestern and northwestern USA[13]; eastern China and the Tibetan plateau[14] (Fig. 2).

To assess the robustness of our gridded reconstruction we conducted a number of validation tests. Recognizing the potential for low-resolution, less well dated, proxies to introduce temporal biases in the reconstruction, we produced a decadally resolved reconstruction from an even more strictly screened subset of proxies (Methods). At the grid point level the median correlation between the full reconstruction and the decadally resolved reconstruction is $r=0.97$ ($p<0.01$). Additional sensitivity tests, for example, excluding one proxy type at a time, excluding or retaining records according to their seasonal signal, or their resolution (Methods; Extended Data Table 1), also reaffirm the robustness of the full reconstruction. Moreover, our reconstruction shows a relatively good correlation with tree-ring-derived reconstructions of PDSI, despite the differences between metrics and reconstruction seasonality (Methods; Extended Data Table 1)[20,21]. We also compared our decadal reconstruction to decadal means of gridded instrumental precipitation data over the twentieth century. The median correlation is $r=0.66$ ($p<0.05$), but the short length of the instrumental data precludes a full validation of the low-frequency behaviour in our hydroclimate reconstruction (Methods; Extended Data Figs 2 and 3).

In regions with sufficient overlap between the hydroclimate and temperature reconstructions, we observe a tendency for wetter conditions during warmer periods in northern Europe, the eastern Mediterranean, Greenland, northern China, northwestern North America and the southeastern USA (Extended Data Fig. 4c, d). Drier conditions during warmer periods are seen in the central Mediterranean, central and northeastern North America, southwestern USA, and southern China. For certain regions (for example, northern China, northwestern North America, northern Europe and Greenland) the patterns of covariance between reconstructed temperature and hydroclimate are qualitatively consistent with the predicted signature of hydroclimate changes under future global warming[3,4,7,18,19].

With our new spatial hydroclimate reconstruction we evaluated the centennial distributions of gridded hydrological and temperature anomalies (Fig. 3) against an identical extraction of precipitation and temperature anomalies from six state-of-the-art coupled atmosphere–ocean general circulation model simulations covering the period 850–2005 (Table 1; Fig. 2c; Extended Data Figs 4a, b and 5). Both the proxy and model data agree that the thirteenth century had the most extensive dry conditions in the pre-industrial period. We observe that the seventeenth century, the coldest Northern Hemisphere century of the past twelve centuries in both proxy and model data (Extended Data Fig. 6a, b)[15,17], shows hydrological conditions close to the long-term mean, with a lack of extremes (only 6% reconstructed hydroclimate anomalies exceeding ± 0.5).

Overall, large-scale agreement in the temporal evolution between proxy and model anomaly distribution characteristics is observed from the tenth to the eighteenth centuries for both hydroclimate and

Table 1 | Models used in this study from CMIP5, with simulations from 850 to 2005

Abbreviated model name	Model institute	Atmospheric resolution (longitudinal x latitudinal)	Forcing
bcc-csm1-1	Beijing Climate Center, China	$2.81° \times 2.81°$	ref. 23
CCSM4	National Center for Atmospheric Research, US DOE/NSF, USA	$1.25° \times 0.9°$	ref. 23
GISS-E2R	NASA Goddard Institute for Space Studies, USA	$2.5° \times 2°$	ref. 23
HadCM3	Hadley Center, UK Met Office, UK	$3.75° \times 1.875°$	ref. 23
IPSL-CM5A-LR	Institute Pierre Simon Laplace, France	$3.75° \times 1.89°$	ref. 23
MPI-ESM-P	Max Planck Institute for Meteorology, Hamburg, Germany	$1.875° \times 1.875°$	ref. 23

CMIP5, Climate Model Intercomparison project Phase 5. For references to the individual models and additional information, see Methods.

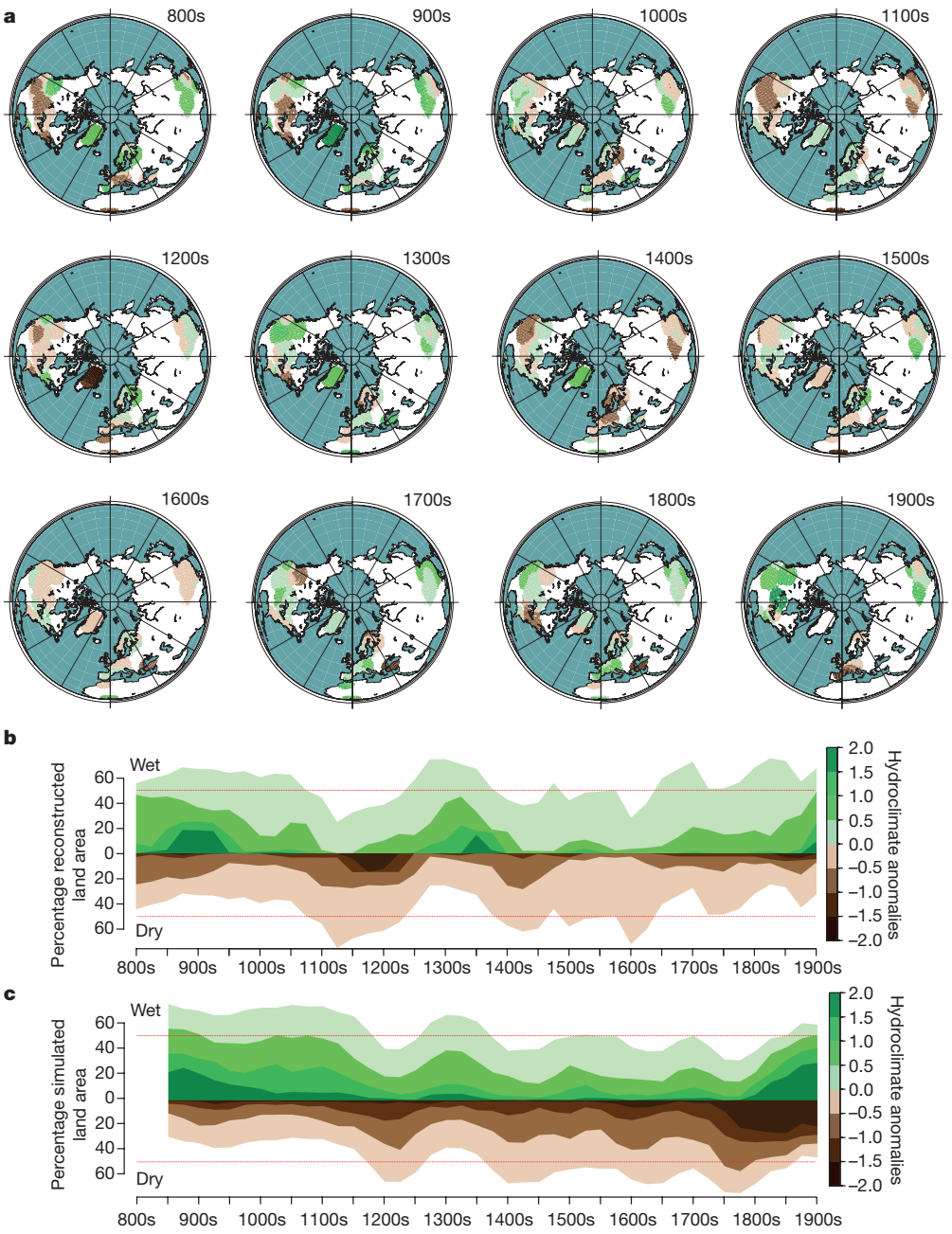

Figure 2 | Spatial-temporal distribution of gridded centennial hydrological proxy anomalies. a, Gridded, weighted, centennial hydroclimate proxy anomalies, derived from the proxy data shown in Fig. 1a, over land areas with at least three independent proxies within the estimated centennial correlation decay length for centennial-scale hydrological variability. **b**, Time series derived from the reconstructed gridded weighted hydroclimate anomalies, showing the fraction of land area exceeding a given wetness or dryness threshold. The red horizontal bars denote the 50% levels. **c**, The same as **b** but for median-model anomaly values of annual precipitation. All anomalies are shown relative to the centennial mean and standard deviation over the eleventh to the nineteenth centuries. The colour scale is truncated at −2 and 2 and areas with insufficient proxy coverage to compute a gridded weighted mean value are left white.

temperature (Fig. 3). However, the similarities in reconstructed and simulated hydroclimate begin to break down in the nineteenth century, with outstanding disagreement of the centennial distribution characteristics in the twentieth century. The proxy data continue to show hydroclimate characteristics in the twentieth century similar to those in the pre-industrial era, whereas the models simulate a high percentage (36.8%) of the land areas to be in either an extremely dry (21.4% of anomalies <-1.5) or extremely wet (15.4% of anomalies >1.5) state. In contrast to the simulations, the proxy data show more extreme hydroclimate anomalies during centuries other than the twentieth (Figs 2 and 3). The unprecedented intensification of wet and dry anomalies in the model simulations, presumably driven by anthropogenic forcing, results in an exceptionally strong meridional gradient producing a wetter north and drier south (Fig. 2; Extended Data Fig. 7a–f) not found in the proxy data. This produces a distinct bimodal distribution of simulated hydroclimate (that is, wet and dry extremes), whereas the proxy data reveal a unimodal distribution both in the industrial and pre-industrial period (Fig. 3). Assessment of interdecadal hydroclimate trends and their variances, in proxy and model data, shows that the differences in the twentieth century between proxy and model data are mainly restricted to the centennial-scale mean anomaly. The model and proxy data agree that neither the interdecadal variability nor the decadal trends in the twentieth century are unprecedented (Supplementary Tables 5 and 6).

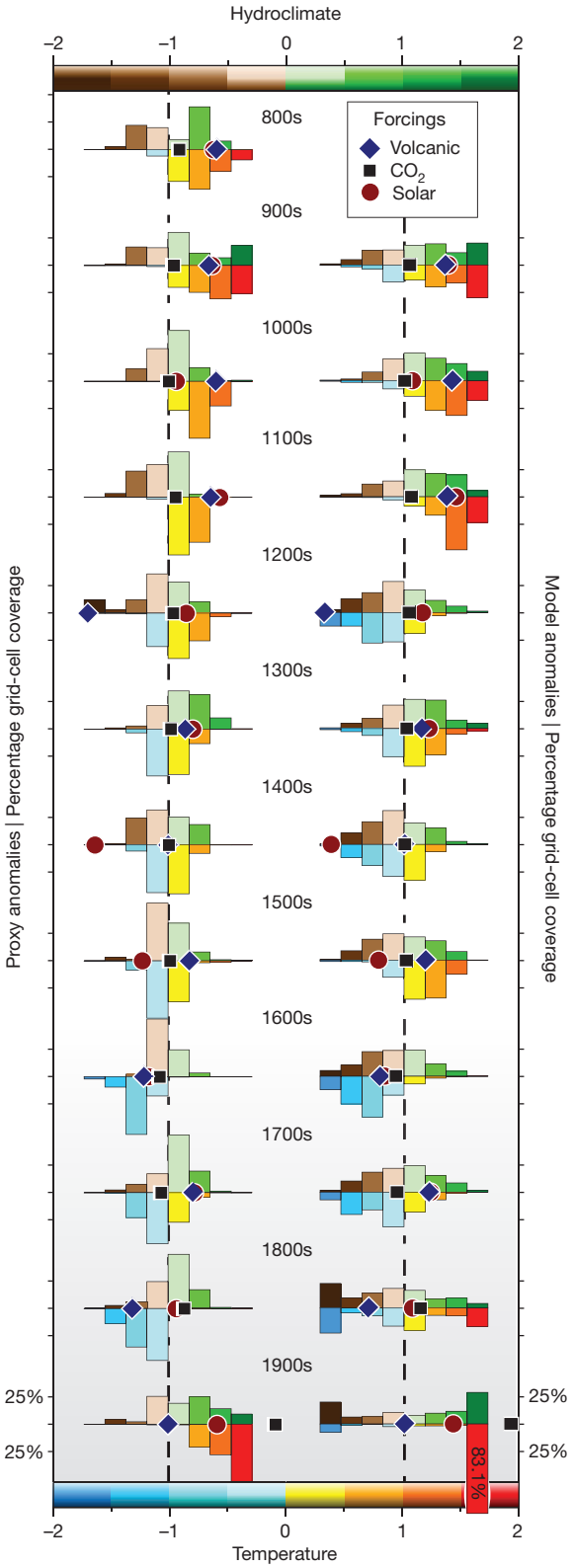

Figure 3 | Probability density function of reconstructed and simulated Northern Hemisphere hydroclimate and temperature anomalies. Reconstructed weighted-smoothed gridded proxy (left) and median-model (right) centennial anomaly values of Northern Hemisphere hydroclimate (top) and temperature (bottom), showing the percentages of Northern Hemisphere land area within defined threshold values ranging from −2 to +2 in increments of 0.5 standard normal deviates. Superimposed on each distribution are the corresponding centennial anomalies of solar, volcanic, and CO_2 forcing time-series (Methods).

A persistent link has been suggested between Northern Hemisphere thermal conditions and the displacement of the Intertropical Convergence Zone (ITCZ)[24]. During warmer periods the ITCZ moves northward, changing the position of Northern Hemisphere storm tracks, monsoon activity and precipitation patterns[25]. A hypothesized mechanism for these changes is an expansion of the Hadley circulation, bringing more moisture and latent energy northward. When we assess the reconstructed hydroclimate patterns during the reconstructed warmest (tenth) and coldest (seventeenth) pre-industrial centuries in the Northern Hemisphere, we find evidence for strong and weak, respectively, meridional gradients supporting the proposed dynamics. In our reconstruction, the twentieth-century manifestation of these dynamics cannot be seen to the extent reconstructed in the tenth century or in the twentieth century in model simulations (Fig. 2b, c; Extended Data Fig. 7). These findings could corroborate the suggestion by ref. 24 that ITCZ migration, owing to anthropogenic greenhouse gas forced warming and possibly tropospheric aerosols, may produce a hydroclimate regime that differs from past regimes. An alternative explanation is that the spatial signature of hydroclimate can be highly variable under comparable thermal conditions, making it difficult to attribute a particular external forcing to the observed patterns.

There are several possible explanations for the limited ability of climate models to simulate hydroclimate variability accurately: knowledge gaps in describing physical processes defining model sub-grid parameterizations[6,26], systematic absolute temperature biases in the models affecting evaporation and precipitation processes[27], and an underestimation of internal hydroclimate variability[28]. We find only limited regional-scale reconstruction–model agreement (Fig. 2a–c and Extended Data Fig. 4a, b), as would be expected if Northern Hemisphere hydrological variability is driven more by internal dynamics than external forcing.

Our comparison of the distribution characteristics and large-scale temporal evolution of reconstructed and simulated centennial-scale hydroclimate reveals strong similarities up to the nineteenth century. However, the proxy evidence does not support the tendency in simulations for wet regions to become wetter and dry regions drier in a warmer climate[29,30]. Furthermore, our hydroclimate reconstruction does not support a general unprecedented intensification of the hydrological cycle in the twentieth century, associated with both more extreme wet and dry conditions, as simulated by an ensemble of models. This finding is in line with recent analyses of instrumental data reporting limited evidence for an intensification of wet and dry anomalies under current global warming[8,9,26]. Absence of evidence for this predicted hydroclimate response to higher temperatures suggests that either the warming in the twentieth century has not been strong enough for this fingerprint to emerge, or that the triggers for the mechanisms responsible should be revised. We conclude that a millennium-long perspective, as provided by multi-proxy evidence, is crucial to our ability to benchmark and evaluate[16,17] hydroclimate simulations accurately.

Online Content Methods, along with any additional Extended Data display items and Source Data, are available in the online version of the paper; references unique to these sections appear only in the online paper.

Received 27 April 2015; accepted 6 February 2016.

1. D'Odorico, P. & Bhattachan, A. Hydrologic variability in dryland regions: impacts on ecosystem dynamics and food security. *Phil. Trans. R. Soc. Lond. B* **367,** 3145–3157 (2012).
2. Field, C. B. *et al.* (eds) *Climate Change 2014: Impacts, Adaptation, and Vulnerability. Part A: Global and Sectoral Aspects. Contribution of Working Group II to the Fifth Assessment Report of the Intergovernmental Panel on Climate Change* (Cambridge Univ. Press, 2013).
3. Cook, B. I., Smerdon, J. E., Seager, R. & Coats, S. Global warming and 21st century drying. *Clim. Dyn.* **43,** 2607–2627 (2014).
4. Schewe, J. *et al.* Multi-model assessment of water scarcity under climate change. *Proc. Natl Acad. Sci. USA* **111,** 3245–3250 (2014).
5. Held, I. M. & Soden, B. J. Robust responses of the hydrological cycle to global warming. *J. Clim.* **19,** 5686–5699 (2006).

6. Stephens, G. L. *et al.* Dreary state of precipitation in global models. *J. Geophys. Res.* **115,** D24211 (2010).
7. Collins, M. *et al.* In *Climate Change 2013: The Physical Science Basis* (eds Stocker, T. F. *et al.*) 1029–1136 (Cambridge Univ. Press, 2013).
8. Sheffield, J., Wood, E. F. & Roderick, M. L. Little change in global drought over the past 60 years. *Nature* **491,** 435–438 (2012).
9. Greve, P. *et al.* Global assessment of trends in wetting and drying over land. *Nature Geosci.* **7,** 716–721 (2014).
10. O'Gorman, P. & Schneider, T. The physical basis for increases in precipitation extremes in simulations of 21st-century climate change. *Proc. Natl Acad. Sci. USA* **106,** 14773–14777 (2009).
11. Orlowsky, B. & Seneviratne, S. I. Elusive drought: Uncertainty in observed trends and short- and long-term CMIP5 projections. *Hydrol. Earth Syst. Sci.* **17,** 1765–1781 (2013).
12. Xoplaki, E., González-Rouco, J. F., Luterbacher, J. & Wanner, H. Wet season Mediterranean precipitation variability: influence of large-scale dynamics and predictability. *Clim. Dyn.* **23,** 63–78 (2004).
13. Steinman, B. *et al.* Ocean–atmosphere forcing of centennial hydroclimate variability in the Pacific Northwest. *Geophys. Res. Lett.* **41,** 2553–2560 (2014).
14. Chen, J. *et al.* Hydroclimatic changes in China and surroundings during the Medieval Climate Anomaly and Little Ice Age: spatial patterns and possible mechanisms. *Quat. Sci. Rev.* **107,** 98–111 (2015).
15. Ljungqvist, F. C., Krusic, P. J., Brattström, G. & Sundqvist, H. S. Northern Hemisphere temperature patterns in the last 12 centuries. *Clim. Past* **8,** 227–249 (2012).
16. Braconnot, P. *et al.* Evaluation of climate models using palaeoclimatic data. *Nature Clim. Change* **2,** 417–424 (2012).
17. Masson-Delmotte, V. *et al.* in *Climate Change 2013: The Physical Science Basis. Contribution of Working Group I to the Fifth Assessment Report of the Intergovernmental Panel on Climate Change* (eds Stocker, T. F. *et al.*) 383–464 (Cambridge Univ. Press, 2013).
18. Trenberth, K. Changes in precipitation with climate change. *Clim. Res.* **47,** 123–138 (2011).
19. Dai, A. Increasing drought under global warming in observations and models. *Nature Clim. Change* **3,** 52–58 (2012).
20. Cook, E. R., Woodhouse, C. A., Eakin, C. M., Meko, D. M. & Stahle, D. W. Long term aridity changes in the western United States. *Science* **306,** 1015–1018 (2004).
21. Cook, E. R. *et al.* Asian monsoon failure and megadrought during the last millennium. *Science* **328,** 486–489 (2010).
22. Evans, M. N., Smerdon, J. E., Kaplan, A., Tolwinski-Ward, S. E. & González-Rouco, J. F. Climate field reconstruction uncertainty arising from multivariate and nonlinear properties of predictors. *Geophys. Res. Lett.* **41,** 9127–9134 (2014).
23. Schmidt, G. A. *et al.* Climate forcing reconstructions for use in PMIP simulation of the last millennium (v1.1). *Geosci. Model Dev.* **5,** 185–191 (2012).
24. Broecker, W. S. & Putnam, A. E. Hydrologic impacts of past shifts of Earth's thermal equator offer insight into those to be produced by fossil fuel CO_2. *Proc. Natl Acad. Sci. USA* **110,** 16710–16715 (2013).
25. Schneider, T., Bischoff, T. & Haug, G. H. Migrations and dynamics of the intertropical convergence zone. *Nature* **513,** 45–53 (2014).
26. DeAngelis, A. M., Qu, X., Zelinka, M. D. & Hall, A. An observational radiative constraint on hydrologic cycle intensification. *Nature* **528,** 249–253 (2015).
27. Mauritsen, T. *et al.* Climate feedback efficiency and synergy. *Clim. Dyn.* **41,** 2539–2554 (2013).
28. Zhang, X. *et al.* Detection of human influence on twentieth-century precipitation trends. *Nature* **448,** 461–465 (2007).
29. Allan, R. P. & Soden, B. J. Atmospheric warming and the amplification of precipitation extremes. *Science* **321,** 1481–1484 (2008).
30. Polson, D., Hegerl, G., Allan, R. & Sarojini, B. B. Have greenhouse gases intensified the contrast between wet and dry regions? *Geophys. Res. Lett.* **40,** 4783–4787 (2013).

Supplementary Information is available in the online version of the paper.

Acknowledgements Funding for this work was provided in part by the Swedish Research Council (grant number C0592401), and the Navarino Environmental Observatory (NEO) (project number 1946322). E.Z.'s contribution is part of the German Cluster of Excellence CLISAP (grant number EXC177). The publication cost was covered by the Bolin Centre for Climate Research, Stockholm University, and the Department of Physical Geography, Stockholm University. This is a contribution to the Past Global Changes (PAGES) 2k Network. We thank U. Büntgen at the Swiss Federal Research Institute WSL, and H. Grudd at the Swedish Polar Research Secretariat, for comments on the manuscript.

Author Contributions F.C.L. and P.J.K. designed the study from an original idea by F.C.L. and P.J.K., with input from H.S.S., E.Z., G.B. and D.F. F.C.L. and P.J.K. collected all the proxy data and H.S.S. screened the records for dating uncertainties. P.J.K. produced the software used for the analyses with input from the co-authors. E.Z. provided the model data and calculated the correlation decay length information. All authors contributed to discussion and interpretation of the results. F.C.L., P.J.K. and D.F. wrote the paper with input from the other co-authors.

Author Information Data and code is digitally archived at the NOAA Paleoclimatology/World Data Center for Paleoclimatology (https://www.ncdc.noaa.gov/paleo/study/19725). Reprints and permissions information is available at www.nature.com/reprints. The authors declare no competing financial interests. Readers are welcome to comment on the online version of the paper. Correspondence and requests for materials should be addressed to F.C.L. (fredrik.c.l@historia.su.se).

METHODS

The proxy data collection. We systematically searched the scientific literature for proxy records of hydroclimate and temperature. We retrieved all records fulfilling the following criteria:

(1) Temporal coverage. All proxy records must cover at least the period 1000–1899.

(2) Temporal resolution. All proxies must have at least, on average, two data points per century between 1000 and 1899 and no more than two centuries over the 1000–1899 period may have fewer. In the data subset containing only hydroclimate records resolved decadally or better, we required that all proxies have, on average, one data point per century between 1000 and 1899.

(3) Publication requirements. We use only proxy records that have been published in the scientific literature.

(4) Requirements regarding the climate signal. The proxies must, according to their published description, contain a hydrological signal described as precipitation, drought, moisture balance, stream flow, lake level change, bog surface wetness, flooding or similar hydrological information.

(5) Geographical requirements. All the proxies must be located in, or nearly in, the Northern Hemisphere. Proxies just south of the Equator (by a few degrees) may be included if they contribute to gridded values north of the Equator.

The majority of records were obtained from public repositories (for example, http://www.ncdc.noaa.gov/paleo/ and http://www.pangaea.de/). Those records not in the public domain were acquired either by direct request from their authors, or digitized from figures in the original articles (Supplementary Tables 1 and 2). The proxy data were divided into seven categories: (1) ice cores, (2) peat cores, (3) tree rings, (4) speleothems, (5) documentary, (6) lake sediments, and (7) marine sediments. In cases where there exist several versions of a proxy record from the same site, preference was given to the latest published version. The collected proxy records were divided into three simplified categories of seasonal response: annual, winter and summer, with spring and early autumn considered as part of the summer season. In cases when no clear information about a proxy's seasonality could be found, either in the original article or in subsequent publications, we assumed the seasonality to be annual.

Geochronological screening. We only included proxy records with age models constrained by at least one dating point after 1900 (D1), another between 1000 and 1900 (D2) and one dating point before 1000 (D3). The number of years between D1 and D2 and D2 and D3 should be less than 1,000 years.

The dating criteria are:

(1) The top of the core exists (that is, year of collection) or, if it does not, there must be a dating point (for example, ^{137}Cs, ^{210}Pb) to verify the age (A1 is the top age).

(2) There should be at least one dating point (^{14}C, U/Th, tephra, ^{210}Pb) between 800 and 1999 (A2).

(3) There should be at least one dating point between 800 and 1 (A3).

(4) The spacing between these three dating points should be less than 800 years (A1 − A2 < 800 years, A2 − A3 < 800 years).

(5) A1, A2 and A3 cannot be bulk datings.

(6) The acceptable dating errors for A1, A2 and A3 must be <200 years (2σ).

For the decadal- or better-resolved subset, each record must have at least one dating point per full century.

Data treatment. Prior to computing centennial anomalies, all proxy records with irregularly spaced time steps were converted into time series with annually spaced time steps using simple linear interpolation, then smoothed by a cubic smoothing spline having a 50% frequency response at 100 years. The smoothed proxy series are transformed to standard normal deviates with respect to the 1000–1899 baseline period. From the resulting centennial anomalies every 25th value is extracted from each century with at least 85 (interpolated) values. From those proxy records spanning the complete 800–1999 period, we obtain 45 centennial anomalies. Of these 45 centennial anomalies the 12 representing the hundred-year periods 800–899, 900–999, 1000–1099, 1100–1199, …, 1900–1999, are those presented in the majority of figures throughout this Letter (Extended Data Fig. 8b). However, all 45 centennial anomalies are used in the correlation experiments as well as in Fig. 2b and c. For the subset including only hydroclimate records decadally resolved or better, we obtained decadal anomalies using the same method as described above but instead using a spline with a 50% frequency response at 10 years.

Correlation decay length. Because individual proxy records can contain noise, a more robust signal is presumably obtained by producing an average of multiple proxies from within a geographic area where hydroclimate can be assumed to be coherent. Unfortunately, the size of such geographic areas, on centennial timescales, is not well constrained owing to the limited length and distribution of instrumental observations. This deficiency required the development of a measure of correlation decay length (CDL)[31] of hydroclimate[32,33] on centennial timescales. Encouraged by the agreement found between instrumental precipitation data on annual and decadal timescales[34] and simulated values from the ECHO-G model[35] on the same timescales, we used the simulated centennial values from the ECHO-G model to calculate a conservative estimate of the spatial auto-correlation function for hydroclimate on centennial timescales by the following equation:

$$C(j,L)=\frac{1}{N}\sum_{i}\left\{\frac{1}{M}\sum_{\substack{t,k,l\\ L-\Delta L\le d\le L+\Delta L}} f(t,i,j)f(t,k,l)\right\} \quad (1)$$

where t is the time index, i and j are the longitude index and the latitude index of the grid, respectively; $f(t, i, j)$ are the deviations from the local long-term mean at time t and at a grid-cell (i, j) divided by the local temporal standard deviation (that is, standardized to one standard deviation), d is the spatial separation between grid cells (i, j) and (k, l). The sum of the product $f(t, i, j)f(t, k, l)$ over time and space is restricted to the grid cells (k, l) that are separated from the grid cell (i, j) by the distance between $L-\Delta L$ and $L+\Delta L$, where ΔL is 100 km. This sum is divided by the number of occurrences of grid-cell pairs. The outer sum is calculated over all grid cells located on an index circle j, and then this sum is divided by that number of grid cells. It is thus assumed that the spatial autocorrelation is isotropic and zonally homogeneous, that is, it depends only on length L and on latitude j. The assumption of isotropy and zonal homogeneity is an assumption that is not completely fulfilled for all terrestrial locations. However, this approach yields an approximate and average estimation of the decorrelation length at multi-decadal to centennial timescales, and this estimation amounts to a few hundred kilometres (Extended Data Fig. 1a). The precise value of the decorrelation length does not affect the basic features of the reconstruction. A simplified CDL function of hydroclimate variability on centennial timescales was derived from the output of the climate model ECHO-G[35] over the period 1000–1990 to calculate the maximum search distances as a function of latitude in this study (Extended Data Fig. 1b).

Averaging, weighting and gridding. We use the distance function described above, derived from the estimated centennial hydroclimate CDL, to define the search radius for averaging proxy anomalies (Extended Data Fig. 1a and b). Finding the decorrelation of hydroclimate increases with distance from a search centre, we assign a weight for each proxy record, for any given latitude, decreasing from 1 at the centre to $e^{-2}\approx 0.14$ at the search periphery using the following Gaussian weight function:

$$w=e^{-2x^2/R^2} \quad (2)$$

Here, w is the weight assigned to a proxy value located at x distance from a grid node, and R is the search radius defined by equation (1). Every reconstructed grid cell location is required to have three or more proxy centennial anomalies within the search radius. This requirement effectively reduces the total number of proxies used in the experiment, although some regions remain densely covered (such as North America, China and Europe; Extended Data Fig. 8a). Weighted means are computed for all 45 centennial anomalies and are those used in the correlation analyses. All gridding and weighting of proxy (and model) data are performed using the method described above for producing the proxy local weighted averages, although the search area centres are moved to each intersection of a 1° × 1° longitude by latitude grid superimposed over a polar projection of the Northern Hemisphere. Maps of centennial gridded proxy hydroclimate variability are shown in Fig. 2a, and time series corresponding to the fraction of land area at or above a given wetness or dryness threshold are shown in Fig. 2b. The weighted and gridded proxy temperature reconstruction shown in Extended Data Fig. 6a and used in Fig. 3 is produced in the same manner as the hydroclimate reconstructions, with the exception of the CDL function used for weighting and gridding. Detailed descriptions of the CDL, the proxy weighting function, and the search distance function used for reconstructing Northern Hemisphere centennial temperature variations are given in ref. 15.

Climate model data. We have used simulations from six coupled atmosphere–ocean general circulation model simulations that are part of the Climate Model Intercomparison project Phase 5 (CMIP5)[36]. The simulations denoted as 'past1000' cover the period 850–1850, whereas the 'historical' simulations cover the period 1851–2005. The 'past1000' simulations are sometimes performed using a lower resolution or simplified versions of the more comprehensive models used for the 'historical' simulations. We have restricted our analysis to those six simulations—bcc-csm1-1[37], CCSM4[38], IPSL-CM5A-LR[39], GISS-E2R[40], HadCM3[41], and MPI-ESM-P[42]—conducted with the same model versions for both periods and stitch the 'past1000' and 'historical' simulations that carry the same ensemble run-initialisation-physics (rip) identifier in the CMIP5 repository (Table 1). However, the simulation conducted with the MIROC-ESM model was not used owing to a documented, unrealistic, long-term positive temperature trend in global mean annual near-surface temperature over the past millennium[43].

The models were driven by estimations of external forcing, including variations in the orbital changes, total solar irradiance, volcanism, atmospheric trace

gases and land-use changes. The CMIP5 Consortium recommended similar, but somewhat different, options for these external forcings[23,44] and the modelling groups did not always use the same options for all CMIP5 simulations. From each of the six simulations we extracted the annual mean precipitation and temperature at the model grid-cell location nearest to our proxy locations. Once the selection was made, an equal length extraction was performed to make all comparisons between model and proxy as equitable as possible. The smoothing, weighted averaging and gridding of all model data followed the same protocol as described above for the proxy data. The centennial forcing anomalies in Fig. 3 are produced from time series of solar[45], volcanic[46] and CO_2 forcing[47] the same or similar to those used in the models.

Calculation of correlations. All temporal correlations between two weighted and gridded data sets are calculated by Pearson product-moment correlation coefficient[48]. Assessment of the statistical significance of these correlations is complicated by the fact that any two data sets are both temporally and spatially correlated. We have taken temporal correlation, that is, autocorrelation, into account by using the method of blocked bootstrap (3,001 repetitions)[49] to provide a more realistic estimate of the correlation's statistical significance. In Extended Data Fig. 4a we show the correlations between the gridded hydroclimate proxy data and corresponding gridded hydroclimate model data and Extended Data Fig. 4b shows the statistical significance of the correlations. In Extended Data Fig. 4c we show the correlations between the gridded hydroclimate proxy data and gridded temperature proxy data and Extended Data Fig. 4d shows the statistical significance of the correlations.

We produce histograms of all cross-correlations in this study (Extended Data Fig. 9a–d) and their Fisher z transform[50] (Extended Data Fig. 9e–h) to assess the normality of their distributions. A slightly bimodal distribution is seen, for both the original and Fisher z-transform correlations, between the gridded hydroclimate proxy data and gridded temperature proxy data. This is not what we would expect to see if hydrological and temperature anomalies were unrelated: the distribution of the Fisher z transform of the correlations should then be approximately normal and, in particular, unimodal. Instead, the histograms suggest that the distributions of the correlations between proxy hydroclimate and proxy temperature values are a mixture of two unimodal distributions, corresponding to two distinct mechanisms relating hydroclimate and temperature.

Validation tests. To assess the robustness of our gridded weighted hydroclimate reconstruction we have produced a number of 'subset' reconstructions, using different data screening schemes, as well as comparing our multi-proxy reconstruction to other hydroclimate products. We created a subset of proxies with only those records that have decadal to annual resolution and at least one dating point per century. The gridded reconstruction obtained from this subset has less spatial coverage than the reconstruction from the full data set. The median Pearson product-moment correlation coefficient, at grid point level, between the two reconstructions (using 45 centennial values, lagged by 25 years) is $r = 0.97$ ($p < 0.01$), suggesting that any potential dating uncertainties that exist in the full data set have a small influence on our overall results (Extended Data Table 1). Furthermore, we correlated the full reconstruction with reconstructions produced excluding one of the seven proxy types at the time, which notably also involves excluding the numerous but less well age-constrained lake sediment records (Extended Data Table 1).

Moreover, we produced similar tests excluding/retaining proxy records reflecting quantitative estimates of precipitation as well as excluding/retaining proxy records with annual signal, summer signal, and winter signal, respectively. Finally, we correlated our reconstruction from the full data set as well as the reconstruction from the more strictly screened data set resolved decadally or better, set against the North American Drought Atlas[20] and the Monsoon Asia Drought Atlas[21]. At grid point level the median Pearson's correlation is $r = 0.34$ ($p < 0.15$) and $r = 0.50$ ($p < 0.03$), respectively. These significant, but not very high, correlation values are acceptable considering our hydroclimate reconstruction metric is not an equivalent measure of the PDSI[51,52] and furthermore that the PDSI reconstructions are for the summer season only.

Potential spectral biases in proxy data. The Earth's climate system contains variability from sub-daily to Milankovitch to deep geological timescales[17,53–55]. It has been known for a long time that proxy records may record climatic variation occurring on different wavelengths (that is, interannual to decadal to centennial to millennial) with varying fidelity resulting in disproportionate manifestations of the variance across these different wavelengths[56–62]. Such 'spectral biases' are a type of noise that, if not considered or corrected, potentially challenge a precise quantitative assessment of the continuum of climate variability. Using instrumental records to characterize and subsequently correct the possible spectral biases in proxy records should yield more accurate reconstructions of climate. However, we note that this endeavour to characterize proxy biases is questionable, because the true long-term characteristics of the climate system remain broadly unknown, which is part of the motivation to develop high-quality proxy data and reconstructions.

Knowledge of proxy data sets is, however, sufficiently advanced to state that individual proxy types may be characterized by one or more biases. For example, tree-ring data, arguably the most intensively investigated proxy archive for the past millennium in both the temporal and frequency domains, are known to have two potentially opposing biases. On the one hand, owing to a 'biological memory', tree-ring width data especially contain somewhat less high-frequency (interannual) variability than instrumental temperature (or precipitation) data[59–62]. On the other hand, the necessary removal of the long-term age/size-related trends in tree-ring records, if performed using certain techniques, results in the so-called 'segment length curse'[63] that limits our ability to preserve trends/variability exceeding the length of the mean length of the individual tree-ring sequences. In this case, diminished low-frequency (centennial to millennial) variability would be expected.

There are, however, different techniques that can be applied to overcome or mitigate such spectral biases. The removal of the age-related trends using a single population estimate as in the Regional Curve Standardisation technique has been shown to break the 'segment length curse' and to preserve long wavelengths better[63–65]. Similarly, the biological memory can be estimated and removed by autoregressive modelling and the resulting time series can be assigned the spectral properties expected from the instrumental data sets[56]. Analyses of long-term instrumental data sets are limited to the past couple of centuries, which does not, as also mentioned in the main text, allow a full validation of the low-frequency (for example, centennial to millennial timescale) components of proxy data or reconstructions.

In most proxy records, just as with the tree-ring data, the low-frequency variability can be affected by nonlinear processes such as the compression or mixing of layers, a time-varying temperature–precipitation relationship, anthropogenic impacts on the local environment and, in the case of ice-core data, ice-flow movements in the ice cap. It should be noted that the interpolation of non-annual records to annual resolution also results in a spectral bias towards lower frequencies[66]. Given the uncertainties back in time in many individual proxy records, both in the high- and low-frequency signal, a multi-proxy approach, using the average signal from a number of disparate proxy records, is arguably best suited for the study of low-frequency climate variability.

In multi-proxy reconstructions, where the aim is to obtain both the high (annual) and low (centennial) frequency signal, any spectral bias in the proxies, influencing the ratio of the high- and low-frequency signal, is a problem of major importance. Our aim, however, is only to obtain the signal on centennial and longer timescales. By standardizing centennial mean values, proxy records that have both strong and weak low-frequency signals are transformed to records of just centennial-scale information of the same amplitude. This transformation essentially eliminates the influence of spectral biases by making irrelevant whatever prior ratio of high- and low-frequency information had existed in the proxy before standardization. Even if a proxy does not capture the full amplitude of centennial-scale variability (for example, tree-ring width chronologies built by many short individual series and/or limited replication[63]) the impact is small because the standardization process gives all proxies the same amplitude of centennial-scale variability. As long as the proxies have some centennial-scale variability (which is the only variability we retain for our primary reconstruction) the proxies are useful to us.

Our different sensitivity tests (Extended Data Table 1), removing various proxy types from the complete data set and correlating their resulting reconstruction with the full reconstruction, demonstrate a very limited impact of potential spectral biases from particular proxy types on our full reconstruction. These experiments produce remarkably similar hydroclimate reconstructions, suggesting that the purported negative effect of 'mixing' proxies with potential spectral biases is not large (if not altogether mitigated by the standardization). Especially important in this regard are results from those tests in which all the records with less than decadal resolution, with only centennial dating control, and those in which all the tree-ring records and all the lake sediment records are excluded, respectively. Not surprisingly, the reduction in proxy coverage gave rise to some spatially local differences; however, the overall patterns remained the same. Most of the changes seen are less likely to be attributable to spectral biases in the proxies, but rather to a diminishment in the considered number of proxies, and hence greater noise in the reconstruction. We mitigate the impact of proxy noise in our reconstruction approach by requiring multiple records within the search radius for every grid point reconstructed.

Data and code availability. All the proxy data and programs used to perform the experiments herein have been made publicly available at NOAA Paleoclimatology/World Data Center for Paleoclimatology (https://www.ncdc.noaa.gov/paleo/study/19725). The Source Data we used to plot each figure in the Letter are also stored there. The suggested computing environment and dependencies are: Mac OSX 10.6 or greater, Generic Mapping Tools (GMT) 4.5.6 or later[67], Ghostscript 9.10, and Matlab2007b or later. A detailed description of the software used, with example data and runtime commands is supplied with the archived data.

The climate model data included in the simulations of the Climate Model Intercomparison Project Version 5 (CMIP5) can be downloaded from any of the nodes of the Earth System Grid Federation (registration is required and a password is provided after registration), for example from: https://esgf-data.dkrz.de/search/cmip5-dkrz/. The menu on the left side of the page allows the user to select the 'experiment' (in our case, 'past1000' and 'historical'), the model (for example, MPI-ESM-P), the variable (pr = precipitation), and the time frequency (mon = monthly). A click on the search button displays all matching results. The data download can be performed interactively by clicking on the links of the individual files or by downloading a Unix script 'wget', which can be locally run on a Unix computer. All files are written in 'netcdf' format, which also includes the metadata information, and that can be accessed with a variety of software tools, for instance with the public statistical packages R, Climate Data Operators (CDO) or netcdf Operators (NCO). Data of the ECHO-G simulation can be retrieved from the CERA data bank of the German Climate Computing Centre (DKRZ) at http://cera-www.dkrz.de/. An account on the CERA data bank is required to access the data and can be obtained by sending an email to data@dkrz.de. CERA will then provide a personal account and password as soon as possible. Once an account has been created, the data of the ECHO-G simulation can be accessed.

31. Jones, P., Osborn, T. & Briffa, K. Estimating sampling errors in large-scale temperature averages. *J. Clim.* **10,** 2548–2568 (1997).
32. Datta, S., Jones, W. L., Roy, B. & Tokay, A. Spatial variability of surface rainfall as observed from TRMM field campaign data. *J. Appl. Meteorol.* **42,** 598–610 (2003).
33. Wan, H., Zhang, X., Zwiers, F. W. & Shiogama, H. Effect of data coverage on the estimation of mean and variability of precipitation at global and regional scales. *J. Geophys. Res.* **118,** 534–546 (2013).
34. Mitchell, T. D. & Jones, P. D. An improved method of constructing a database of monthly climate observations and associated high-resolution grids. *Int. J. Clim.* **25,** 693–712 (2005).
35. González-Rouco, F., Beltrami, H., Zorita, E. & von Storch, H. Simulation and inversion of borehole temperature profiles in surrogate climates: spatial distribution and surface coupling. *Geophys. Res. Lett.* **33,** L01703 (2006).
36. Taylor, K. E., Stouffer, R. J. & Meehl, G. A. An overview of CMIP5 and the experiment design. *Bull. Am. Meteorol. Soc.* **93,** 485–498 (2012).
37. Xin, X., Wu, T. & Zhang, J. Introduction of CMIP5 simulations carried out with the climate system models of Beijing Climate Center. *Adv. Clim. Change Res.* [in Chinese] **4,** 41–49 (2013).
38. Landrum, L. *et al.* Last millennium climate and its variability in CCSM4. *J. Clim.* **26,** 1085–1111 (2013).
39. Schmidt, G. A. *et al.* Configuration and assessment of the GISS ModelE2 contributions to the CMIP5 archive. *J. Adv. Model. Earth Syst.* **6,** 141–184 (2014).
40. Schurer, A. P., Hegerl, G. C., Mann, M. E., Tett, S. F. B. & Phipps, S. J. Separating forced from chaotic climate variability over the past millennium. *J. Clim.* **26,** 6954–6973 (2013).
41. Dufresne, J.-L. *et al.* Climate change projections using the IPSL-CM5 Earth System Model: from CMIP3 to CMIP5. *Clim. Dyn.* **40,** 2123–2165 (2013).
42. Giorgetta, M. A. *et al.* Climate and carbon cycle changes from 1850 to 2100 in MPI-ESM simulations for the coupled model intercomparison project phase 5. *J. Adv. Model. Earth Syst.* **5,** 572–597 (2013).
43. Sueyoshi, T. *et al.* Set-up of the PMIP3 paleoclimate experiments conducted using an Earth system model, MIROC-ESM. *Geosci. Model Dev.* **6,** 819–836 (2013).
44. Schmidt, G. A. *et al.* Climate forcing reconstructions for use in PMIP simulations of the last millennium (v1.0). *Geosci. Model Dev.* **4,** 33–45 (2011).
45. Steinhilber, F., Beer, J. & Frohlich, C. Total solar irradiance during the Holocene. *Geophys. Res. Lett.* **36,** L19704 (2009).
46. Gao, C., Robock, A. & Ammann, C. Volcanic forcing of climate over the past 1500 years: an improved ice core-based index for climate models. *J. Geophys. Res.* **113,** D23111 (2008).
47. Petit, J.-R. *et al.* Climate and atmospheric history of the past 420,000 years from the Vostok ice core, Antarctica. *Nature* **399,** 429–436 (1999).
48. Pearson, K. Notes on regression and inheritance in the case of two parents. *Proc. R. Soc. Lond.* **58,** 240–242 (1895).
49. Wilks, D. S. Resampling hypothesis tests for autocorrelated fields. *J. Clim.* **10,** 65–82 (1997).
50. Fisher, R. A. Frequency distribution of the values of the correlation coefficient in samples from an indefinitely large population. *Biometrika* **10,** 507–521 (1915).
51. Palmer, W. C. *Meteorological Drought* (US Department of Commerce Research Paper 45, 1965).
52. Dai, A. G., Trenberth, K. E. & Qian, T. T. A global dataset of Palmer drought severity index for 1870–2002: relationship with soil moisture and effects of surface warming. *J. Hydrometeorol.* **5,** 1117–1130 (2004).
53. Lamb, H. H. *Climate: Present, Past and Future* Vols 1 and 2 (Methuen, 1972–1977).
54. Bradley, R. S. *Paleoclimatology: Reconstructing Climates of the Quaternary* (Academic, 1999).
55. Huybers, P. & Curry, W. Links between annual, Milankovitch and continuum temperature variability. *Nature* **441,** 329–332 (2006).
56. Meko, D. M. *Applications of Box-Jenkins methods of time-series analysis to the reconstruction of drought from tree-rings*. PhD dissertation, Univ. Arizona (1981).
57. Guiot, J. The extrapolation of recent climatological series with spectral canonical regression. *J. Climatol.* **5,** 325–335 (1985).
58. Osborn, T. J. & Briffa, K. R. Revisiting timescale dependent reconstruction of climate from tree-ring chronologies. *Dendrochronologia* **18,** 9–25 (2000).
59. Franke, J., Frank, D., Raible, C., Esper, J. & Brönnimann, S. Spectral biases in tree-ring climate proxies. *Nature Clim. Change* **3,** 360–364 (2013).
60. Büntgen, U. *et al.* Tree-ring amplification of the early nineteenth-century summer cooling in central Europe. *J. Clim.* **28,** 5272–5288 (2015).
61. Esper, J. *et al.* Signals and memory in tree-ring width and density data. *Dendrochronologia* **35,** 62–70 (2015).
62. Zhang, H. *et al.* Modified climate with long term memory in tree ring proxies. *Environ. Res. Lett.* **10,** 084020 (2015).
63. Cook, E. R., Briffa, K. R., Meko, D. M., Graybill, D. A. & Funkhouser, G. The 'segment length curse' in long tree-ring chronology development for palaeoclimatic studies. *Holocene* **5,** 229–237 (1995).
64. Esper J., Cook, E. R. & Schweingruber, F. H. Low-frequency signals in long tree-ring chronologies and the reconstruction of past temperature variability. *Science* **295,** 2250–2253 (2002).
65. Esper, J., Cook, E. R., Krusic, P. J., Peters, K. & Schweingruber, F. H. Tests of the RCS method for preserving low-frequency variability in long tree-ring chronologies. *Tree-ring Res.* **59,** 81–98 (2003).
66. Schulz, M. & Stattegger, K. SPECTRUM: Spectral analysis of unevenly spaced paleoclimatic time series. *Comput. Geosci.* **23,** 929–945 (1997).
67. Wessel, P. & Smith, W. H. F. New, improved version of the Generic Mapping Tools released. *Eos* **79,** 579 (1998).

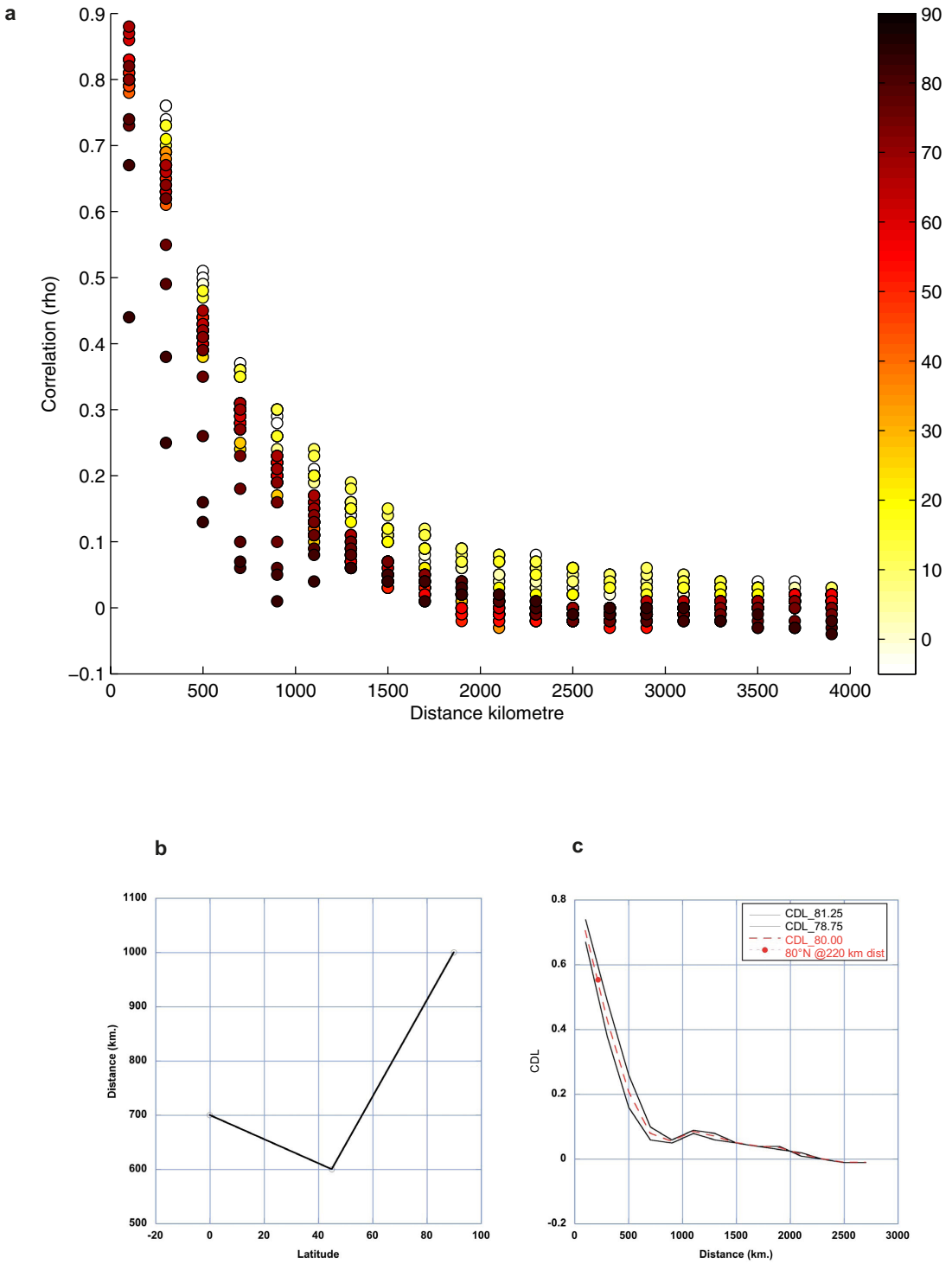

Extended Data Figure 1 | Estimated correlation decay length values. **a**, The spatial decorrelation function ρ for centennial mean precipitation estimated from the output of the climate model ECHO-G[35] over the period 1000–1990, following the procedure described in the Methods for the estimation of the centennial correlation decay length for hydroclimate variability. Distance is the correlation decay length from one point in kilometres. The different colours represent the latitudinal bands. **b**, An example of the estimated spatial autocorrelation function for centennial mean values of precipitation at latitudes 81.25° N, 80.00° N and 78.75° N, respectively, with the decorrelation length for latitude 80° N indicated in red. **c**, The simplified CDL function of hydroclimate variability at centennial timescales, derived from panel **a**, is used throughout the study to calculate the maximum search distances as a function of latitude.

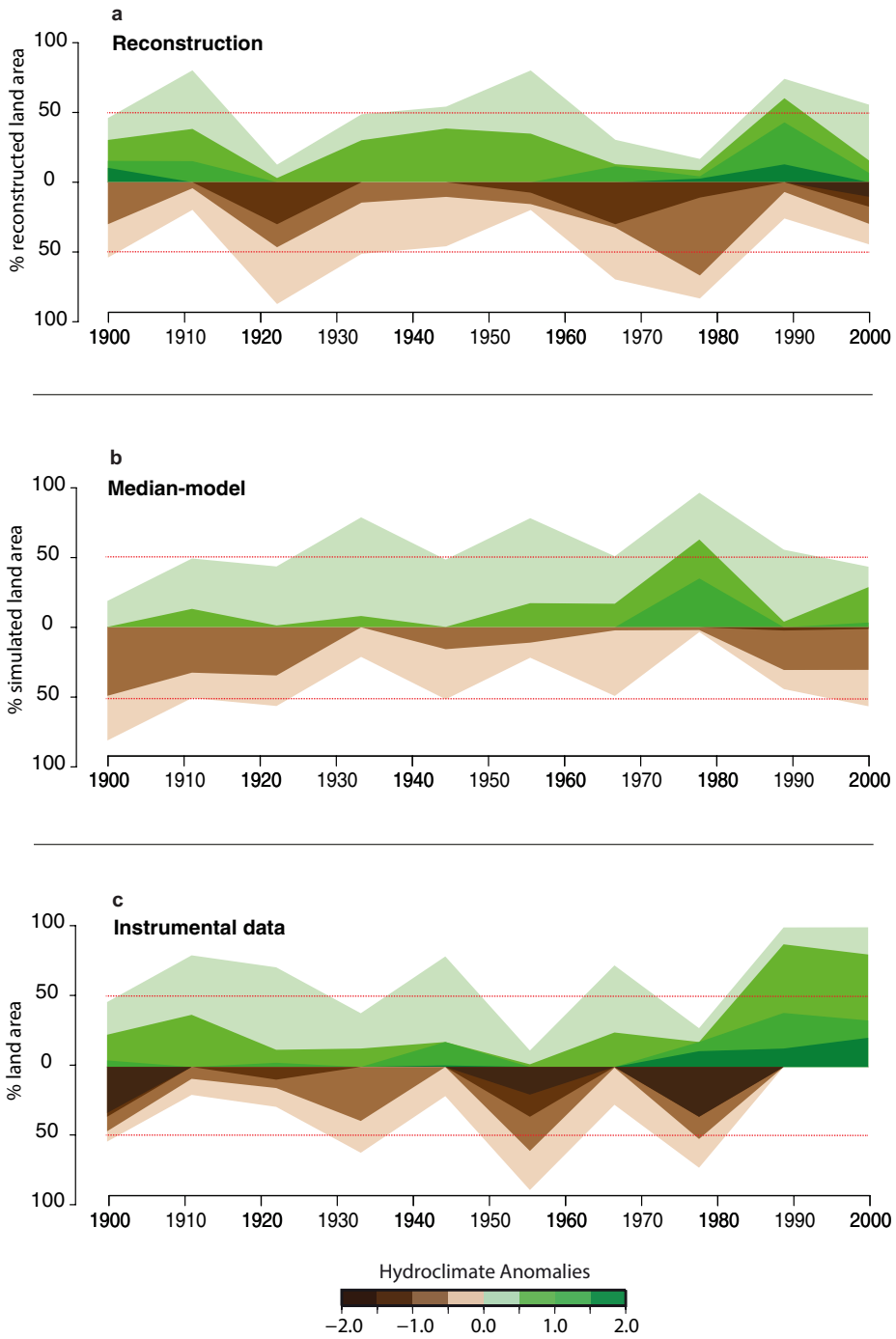

Extended Data Figure 2 | The fraction of land area, expressed as decadal means for 1900–1999, exceeding a given wetness or dryness threshold in the gridded reconstruction, model simulations, and instrumental precipitation data. a, Weighted gridded proxy reconstruction derived from the subset containing only hydroclimate records resolved decadally or better. **b**, The same as **a** but for median-model anomaly values of annual precipitation. **c**, The same as **a** and **b** but for the Global Historical Climatology Network 5° × 5° (GHCN5) instrumental annual precipitation data. All decadal average values are standardized over the 1910–1979 period, and model and instrumental values are extracted from grid cells covered by gridded reconstructed values. The red horizontal bars denote the 50% levels.

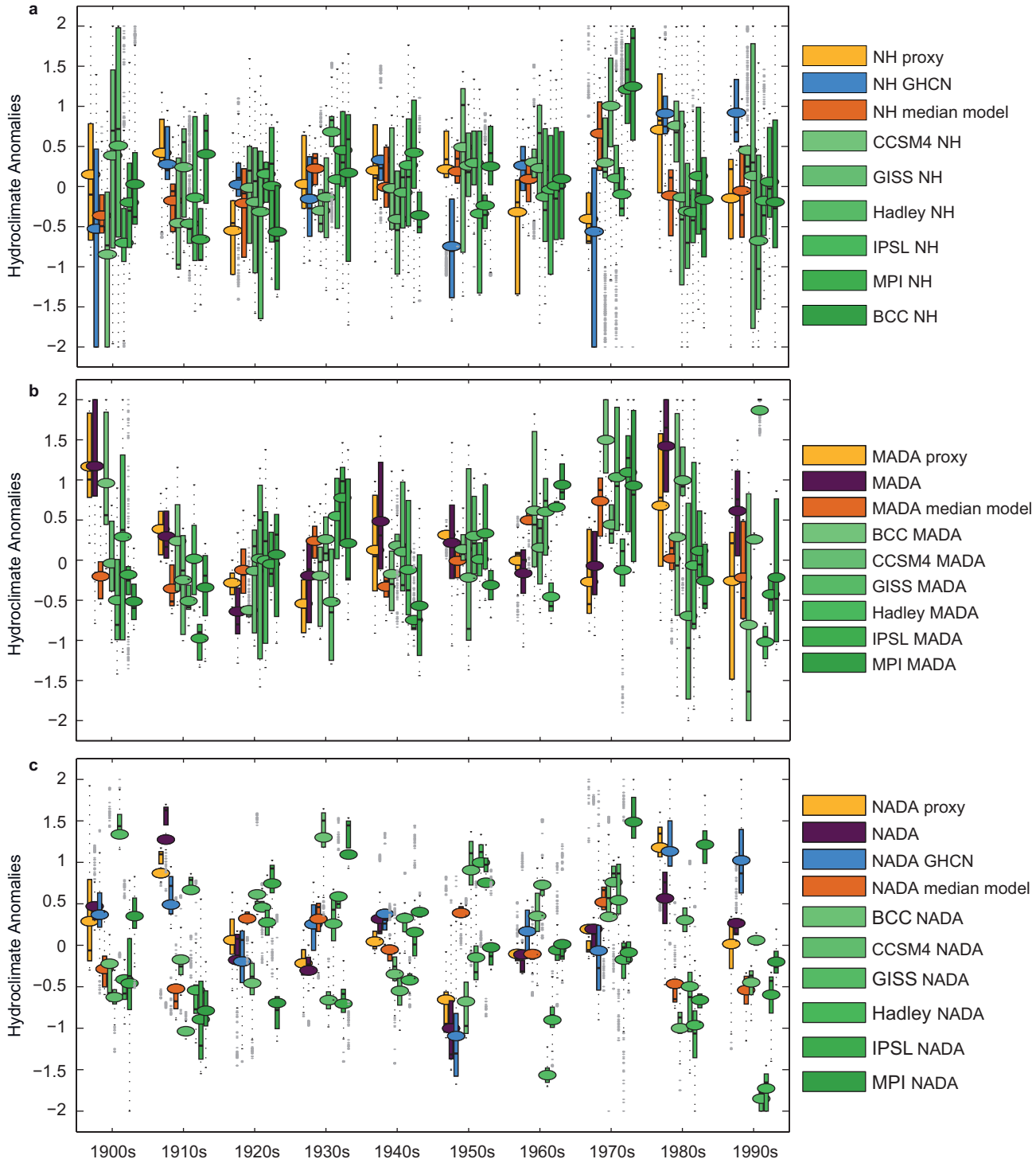

Extended Data Figure 3 | Boxplots showing decadal anomaly values of instrumental data, our gridded reconstruction, drought atlas data, and model simulation of precipitation over the 1900s. a, Comparison of decadal anomalies between our gridded Northern Hemisphere (NH) hydroclimate reconstruction, the gridded 5 × 5° GHCN5 instrumental annual precipitation anomalies, the six individual model simulations (see Table 1) of annual precipitation and their median. **b**, Comparison of decadal anomalies between the Monsoon Asia Drought Atlas (MADA)[21] and the corresponding domain in our gridded Northern Hemisphere hydroclimate reconstruction, the GHCN5 instrumental annual precipitation data set, and in the six individual model simulations of annual precipitation and their median. **c**, Comparison of decadal anomalies between the North American Drought Atlas (NADA)[20] and the corresponding domain in our gridded Northern Hemisphere hydroclimate reconstruction, the GHCN5 instrumental annual precipitation data set, and in the six individual model simulations of annual precipitation and their median. The oval circles represent the mean, the small blank horizontal bar represents the median, the length of the bars represents the quartile range, and the dark grey dots represent the two standard deviation intervals, whereas the light grey dots represent outliers.

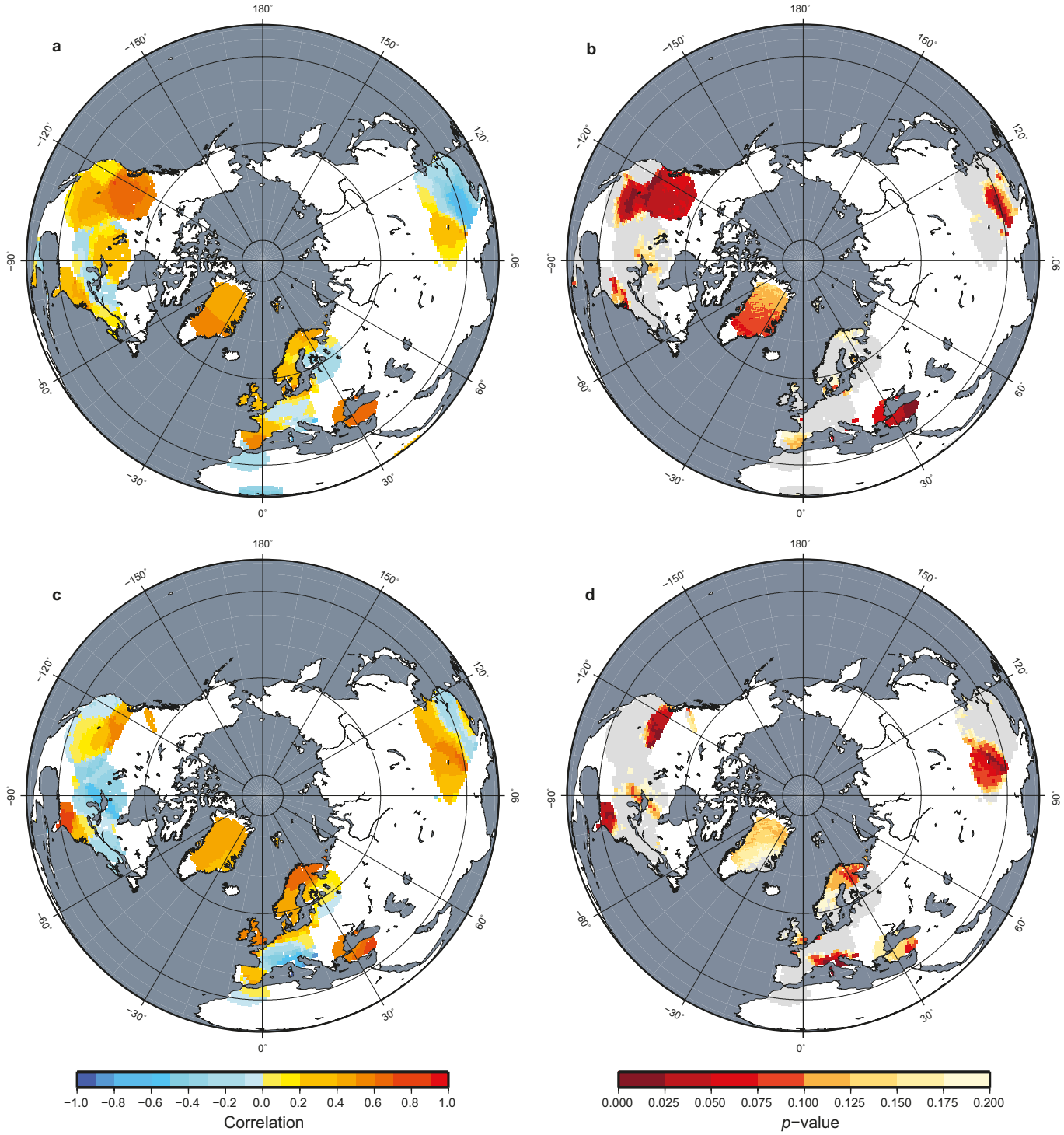

Extended Data Figure 4 | Correlations between gridded proxy and model hydroclimate anomalies, and gridded hydroclimate temperature proxy anomalies. a, Correlations between 45 centennial, lagged 25 years, weighted gridded proxy hydroclimate anomalies and their corresponding median total annual precipitation anomalies from six CMIP5 models, listed in Table 1, over the past twelve centuries. **b**, The Z-transformed block bootstrap *p*-values of the correlations shown in panel **a**. **c**, Correlations between 45 centennial, lagged 25 years, weighted gridded proxy hydroclimate anomalies and weighted gridded proxy temperature anomalies. **d**, The Z-transformed block bootstrap *p*-values of the correlations shown in panel **c**. Areas shown in grey in **b** and **d** have insignificant correlations.

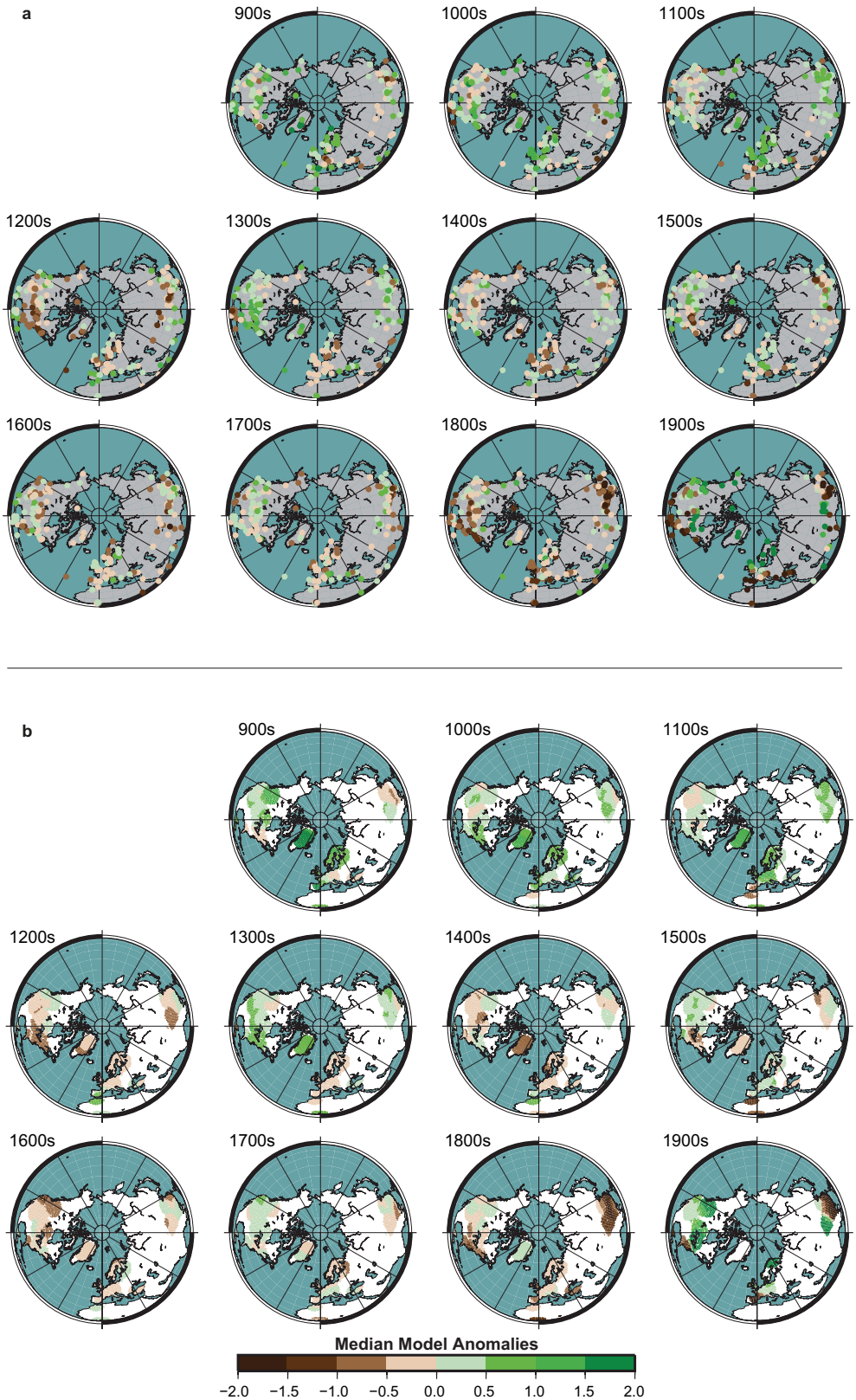

Extended Data Figure 5 | Simulated median values of annual precipitation from six atmosphere–ocean coupled general circulation models. a, Raw, centennial, model anomaly median values calculated and treated and plotted in the same way as the hydrological proxy data. Only values from the same grid cells that are covered by proxy records are extracted (Methods). Anomalies are shown relative to the centennial mean and standard deviation over the eleventh–nineteenth centuries. The colour scale in both panels is truncated at −2 and 2. **b** Gridded, weighted, values for the same data over land areas with at least three independent grid values within the estimated centennial correlation decay length for centennial-scale hydrological variability.

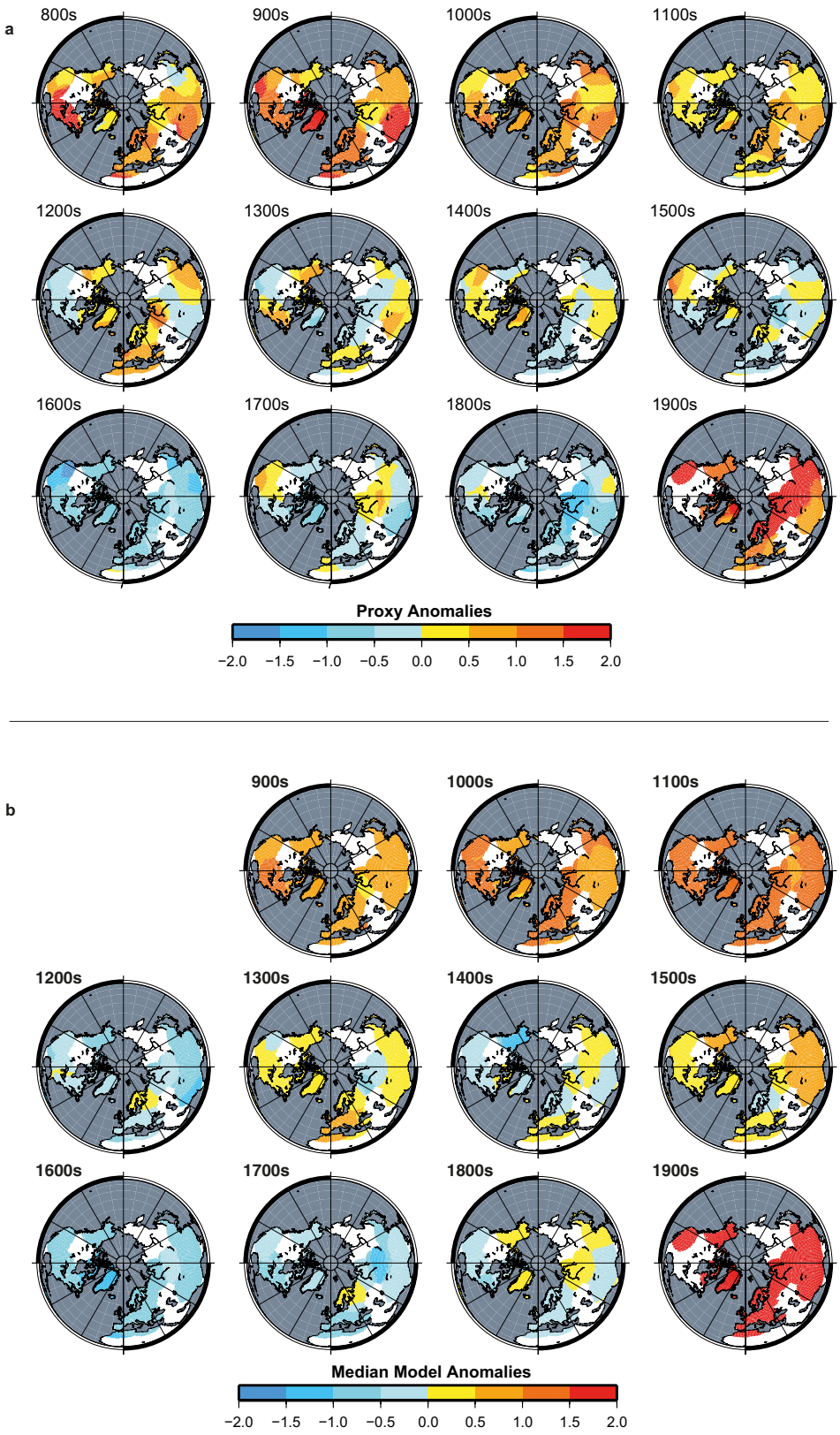

Extended Data Figure 6 | Centennial temperature proxy anomalies updated from ref. 15. a, Gridded, weighted, centennial proxy anomalies values derived from the data listed in Supplementary Table 2 and shown in Fig. 1b. Anomalies are shown relative to the centennial mean and standard deviation over the eleventh–nineteenth centuries. The colour scale is truncated at −2 and 2 and areas with insufficient proxy coverage to compute a gridded weighted mean value are left white. **b**, Gridded, weighted, centennial anomalies for simulated median values of annual mean temperature from six atmosphere–ocean coupled general circulation models. Only values from the same grid cells that are covered by proxy records are extracted (Methods).

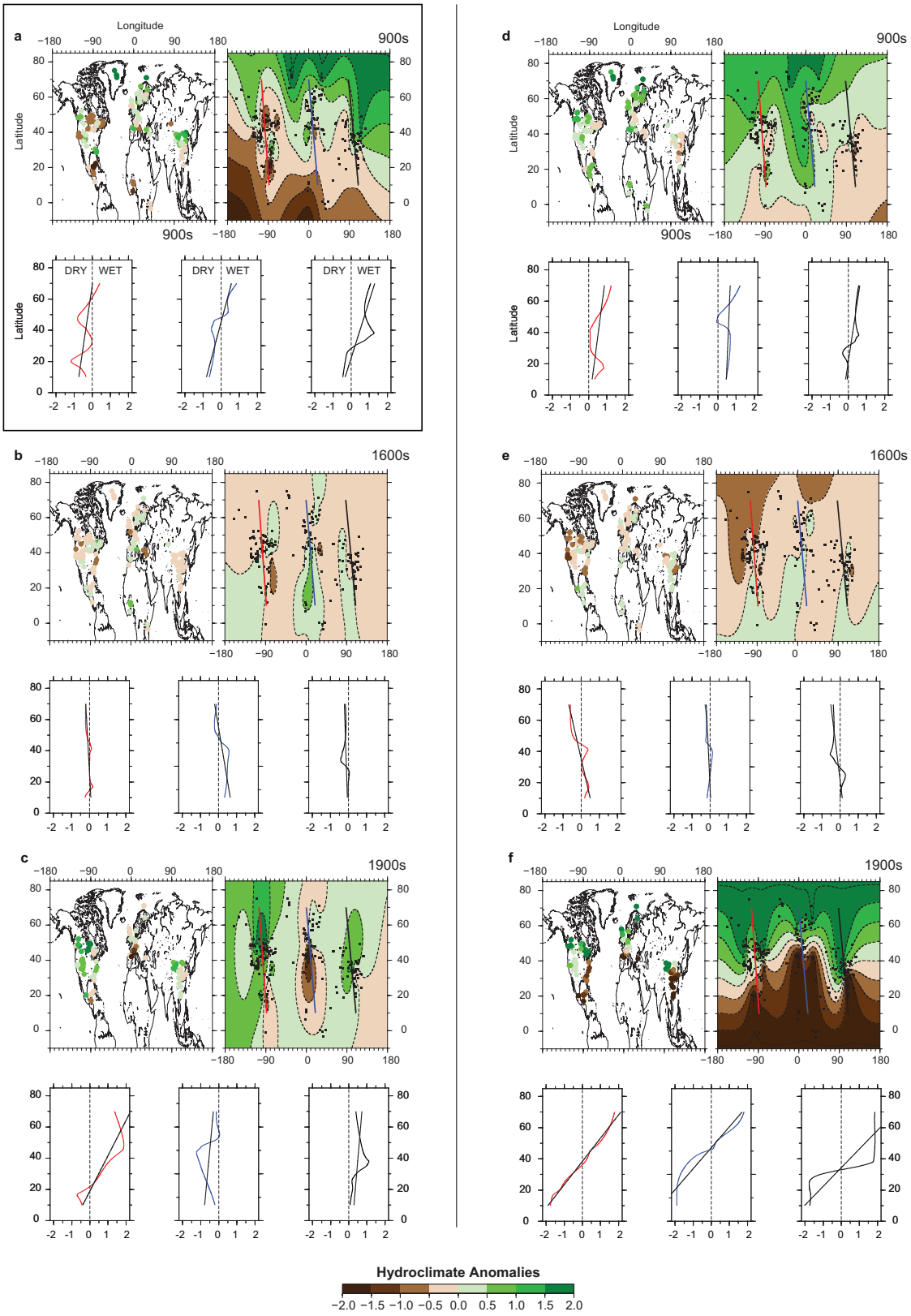

Extended Data Figure 7 | Gradients of proxy-reconstructed and simulated Northern Hemisphere centennial hydroclimate anomalies along three meridional transects for the tenth, twentieth and seventeenth centuries. The tenth and twentieth centuries were the warmest centuries of the past twelve and the seventeenth century was the coldest. **a**, Smoothed, surfaced, and contoured weighted average centennial proxy anomalies for the tenth century (top right). The trend of the smoothed surfaced anomaly values, with their regression line, is shown along the meridional transects, passing through the densest data clusters (red line, North America; blue line, Europe and Africa; and black line, Asia). **b**, **c**, The same as **a** but depicting centennial proxy anomalies of hydroclimate for the seventeenth and the twentieth centuries, respectively. **d**–**f**, The equivalent analysis for the same centennial periods using median-model simulated values, extracted from the same proxy locations, of centennial precipitation anomalies (see Methods).

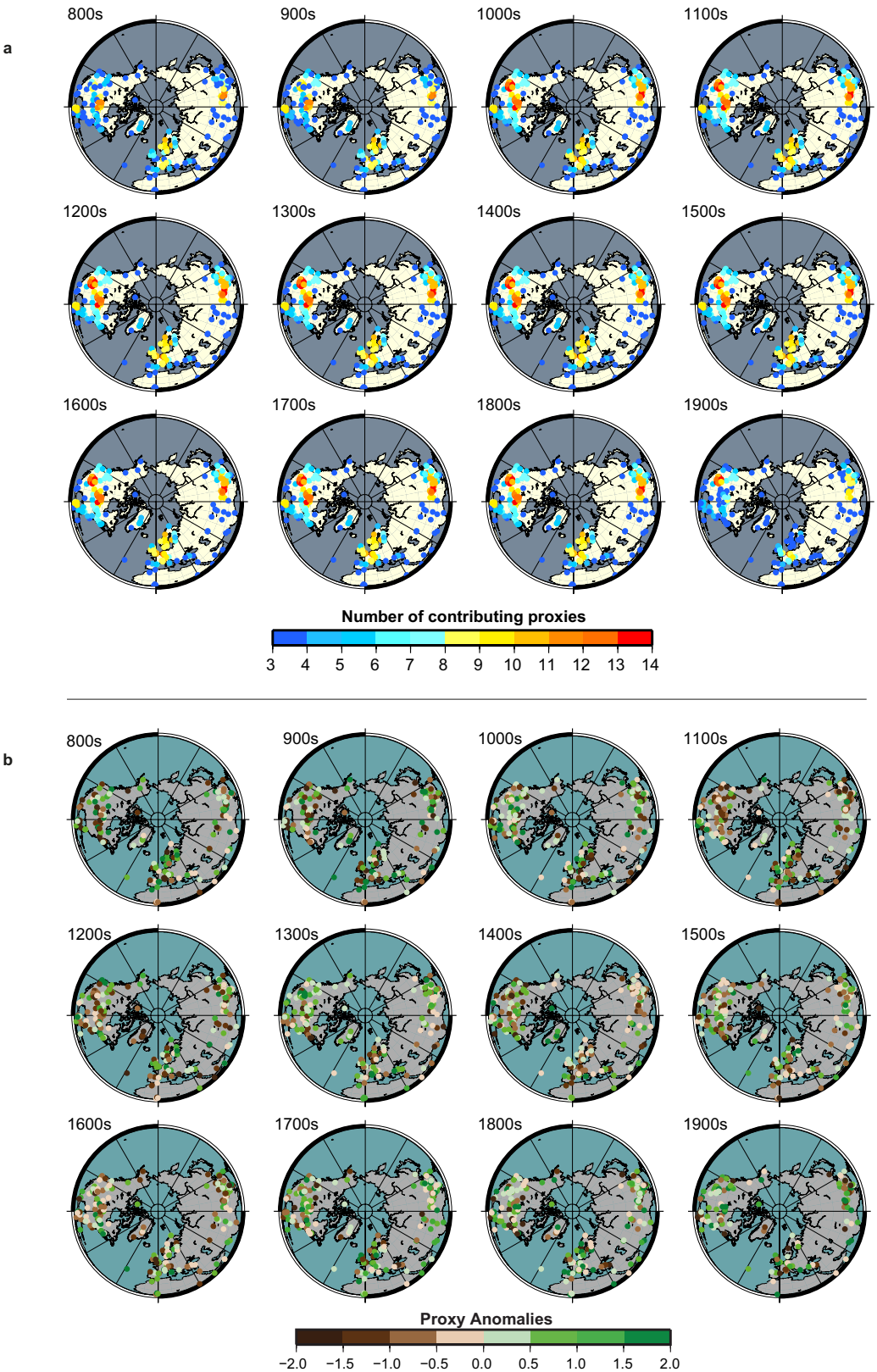

Extended Data Figure 8 | Distribution and density of hydroclimate proxy records. a, Number of contributing hydrological proxy records included in each proxy-centred anisotropic weighted mean calculation where there are three or more neighbouring proxies found in the search radius. **b**, Raw, centennial, hydroclimate proxy anomaly values derived from the data listed in Supplementary Table 1 and shown in Fig. 1a. Anomalies are shown relative to the centennial mean and standard deviation over the eleventh–nineteenth centuries. The colour scale is truncated at −2 and 2 and areas with insufficient proxy coverage to compute a gridded weighted mean value are left white.

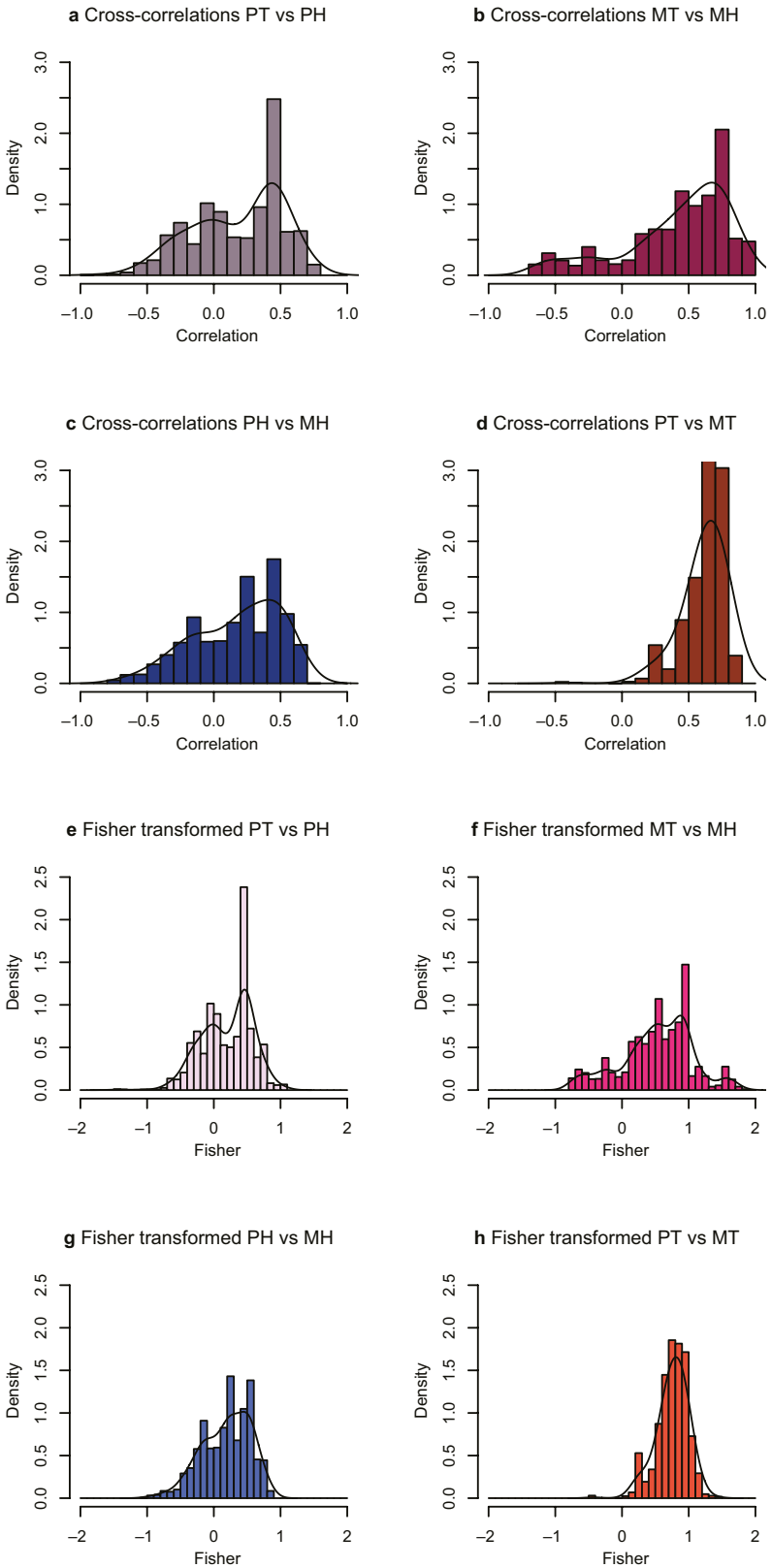

Extended Data Figure 9 | Histograms of cross-correlations with kernel density estimate added. a, Cross-correlations between gridded hydroclimate proxy data and temperature proxy (PT) data. **b**, Cross-correlations between gridded hydroclimate model data and temperature model data. **c**, Cross-correlations between gridded hydroclimate proxy (PH) data and hydroclimate model (MH) data. **d**, Cross-correlations between gridded temperature proxy data and temperature model (MT) data. **e**, The same as **a** but Fisher-transformed. **f**, The same as **b** but Fisher-transformed. **g**, The same as **c** but Fisher-transformed. **h**, The same as **d** but Fisher-transformed. The thin curves in each histogram represent the kernel density estimates.

Extended Data Table 1 | Results from multiple sensitivity tests of our gridded weighted hydroclimate reconstruction

a	Median Pearson's correlation	Median *p*-value
Reconstruction from only records with at least decadal resolution and centennial or better dating control	0.97	< 0.01
Excluding ice cores	0.86	< 0.01
Excluding peat cores	0.90	< 0.01
Excluding tree rings	0.77	< 0.01
Excluding speleothems	0.84	< 0.01
Excluding documentary data	0.90	< 0.01
Excluding lake sediments	0.80	< 0.01
Excluding marine sediments	0.88	< 0.01
Retaining only calibrated precipitation records	0.89	< 0.01
Excluding calibrated precipitation records	0.92	< 0.01
Excluding records with annual signal	0.98	< 0.01
Excluding records with summer signal	0.77	< 0.01
Excluding records with winter signal	0.78	< 0.01
b		
North American Drought Atlas[20]	0.34	0.02
Monsoon Asia Drought Atlas[21]	0.51	< 0.01
c		
GHCN5 instrumental annual precipitation data	0.66	0.05

a, Statistics from correlating the full gridded weighted reconstruction at the grid-cell level with reconstructions derived from using different subsets of proxy data including tests removing one proxy type at the time. **b**, Statistics from correlating the full gridded weighted reconstruction at the grid-cell level with PDSI drought atlas reconstructions. **c**, Results from correlating the decadal-resolved reconstruction from the proxy subset including only records with at least decadal resolution and centennial or better dating control with the decadal mean gridded 5° × 5° GHCN5 instrumental annual precipitation data over the twentieth century.